

Section 1

**Atmospheric data assimilation
schemes, analysis and initialization,
data impact studies, observing system
experiments**

Representation of inhomogeneous, non-separable covariances by sparse wavelet-transformed matrices

Harald Anlauf¹, Andreas Rhodin² and Werner Wergen

Deutscher Wetterdienst, Offenbach, Germany

The purpose of this note is to advocate a new approach to the representation of an NMC- or ensemble-derived, inhomogeneous and non-separable forecast error covariance matrix \mathbf{B} in a global data assimilation system. We use an explicit matrix representation of the covariances on the model grid or on an interpolated auxiliary grid. This approach is actually feasible because realistic NMC-derived covariance matrices have an extremely sparse representation in wavelet transformed space. In contrast to other methods – based on wavelet [1, 2, 3] or spectral transformations – our approach does not attempt to represent covariances by diagonal matrices in the transformed space, but allows for off-diagonal coefficients. The approach is based on orthogonal and bi-orthogonal wavelet transformations corresponding to wavelets with compact support, which can be implemented by fast algorithms [4].

The key idea of this approach is that the relevant information of covariance matrices is contained in a relatively small number of matrix elements. Coefficients accounting for irrelevant information – for instance correlations of small scale phenomena at large spatial separation – may be set to zero a priori. Thus the approach has filter characteristics which should also be useful when applied to forecast ensemble statistics, where filtering of noise – and where increasing the rank of the implied covariance matrices – is essential and generally performed by ‘localization’ procedures based on spatial separation only, but not on the scale of the phenomena.

To obtain a positive-definite, sparse representation of \mathbf{B} we take the symmetric square root $\hat{\mathbf{L}}$ in the wavelet representation, set to zero all coefficients whose absolute value is smaller than a certain threshold, and recalculate $\hat{\mathbf{B}}$.

Figure 1(a) displays the entries of the wavelet-transformed matrix $\hat{\mathbf{L}}$ for the 500 hPa geopotential height correlation at 60°N obtained by the NMC method with zonal averaging and for 256 grid-points. Only a few coefficients of this matrix are substantially different from zero. Furthermore, these nonzero coefficients are essentially located in narrow bands along the diagonal – corresponding to correlations between wavelets of the same scale – and along off-diagonal branches corresponding to correlations between wavelets of different scales but at approximately the same location in grid space.

The grid space correlation function reconstructed from the truncated wavelet representation compares quite well with the original NMC correlation, see fig. 1(b). Of the order of 10 coefficients per grid-point are generally required for a good approximation of 1-dimensional correlations.

Our approach can be generalized to 2 and 3 dimensions. Here we expect of the order of 30 to 100 coefficients per grid-point to be sufficient for a good approximation of the covariance matrix (without taking advantage of redundancy due to symmetry and zonal

¹Email: harald.anlauf@dwd.de

²Email: andreas.rhodin@dwd.de

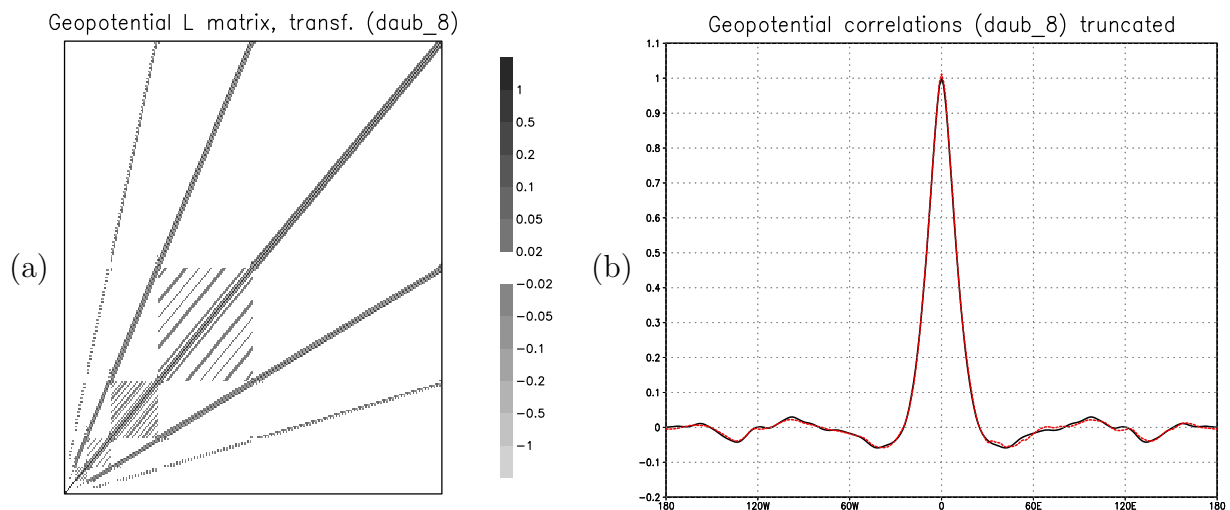


Figure 1: (a) Entries of the wavelet-transformed matrix $\hat{\mathbf{L}}$ for the 500 hPa NMC height correlation (256×256 elements, scaled for unit diagonal elements). (b) Comparison of the NMC correlations (solid black line) with the approximation by the truncated wavelet expansion (keeping only coefficients with absolute value $> 0.5\%$ of the largest one, broken red line).

homogeneity). In 2 and 3 dimensions the suppression of sampling noise due to finite ensemble size and visible as random long-range correlations becomes very important. We are currently implementing and testing a 2d version in the 3D-Var-PSAS under development at DWD.

References

- [1] Mike Fisher, *Generalized Frames on the Sphere, with Application to Background Error Covariance Modelling*, Proc. ECMWF Seminar on Recent Developments in Numerical Methods for Atmosphere and Ocean Modelling, Reading, United Kingdom, ECMWF, 2004, 87-101.
- [2] Alex Deckmyn and Loik Berre, *A Wavelet Approach to Representing Background Error Covariances in a Limited-Area Model*, Mon. Wea. Rev. **133** (2005) 1279-1294.
- [3] R. N. Bannister, *Can Wavelets Improve the Representation of Forecast Error Covariances in Variational Data Assimilation?*, Mon. Wea. Rev. **135** (2007) 387-408.
- [4] Ingrid Daubechies, *Ten Lectures on Wavelets*, CBMS-NSF Regional Conference Series on Applied Mathematics, Vol. 61, SIAM, 1992.
A. Cohen, I. Daubechies, J. C. Feauveau, *Biorthogonal bases of compactly supported wavelets*, Commun. Pure Appl. Math. **45** (1992) 485-560.
A. Cohen, I. Daubechies, P. Vial, *Wavelets on the Interval and Fast Wavelet Transform*, Appl. Comp. Harm. Anal. **1** (1993) 54-81.

The dominant controls on tropospheric hydrology over continental convective regions using isotope measurements from space

Derek Brown and David Noone

*Cooperative Institute for Research in Environmental Sciences (CIRES),
University of Colorado at Boulder, CO, USA (email: derek.brown@colorado.edu)*

The hydrologic regimes of convectively active regions contain intricate balances of large-scale advective supply of water, surface exchange, and atmospheric condensation/evaporation. The isotopic composition provides information about these balances and thus is useful to explore the way hydrology is represented in models, and specifically identify model limitations. To this end, a goal of this work is to explore limitations in General Circulation Model (GCM) hydrology, especially in regions of convection. Although the large-scale control on the isotopic composition of atmospheric moisture is primarily fractionation during evaporation from the oceans, isotopic fractionation during local condensation, evaporation, and evapotranspiration events lead to unique deuterium signals over convectively active regions (Gat, 1996). The seasonal variations in the deuterium content of water vapor seen by the Tropospheric Emission Spectrometer (TES) reflect these changes in convective regimes and give insight into the seasonally dependent influences of land surface conditions on regional hydrologic cycles. In turn, this additional knowledge based on observations can be used to refine parameterized physics in GCMs.

The relative amount of deuterium in a moist air mass is commonly compared to the average deuterium content of seawater and expressed in delta notation as δD (‰). A global map of seasonal differences in airborne δD values (**figure 1**) shows that continental convective regions with well defined monsoon seasons tend to produce the largest seasonal differences in δD values, yet large differences between convective regions of similar latitude exist. Specifically, the Amazon Basin, Asian Monsoon, and Congo regions show more deuterium depletion during their respective wet seasons (DJF for the SH, JJA for the NH), whereas the N. Australia and SW United States regions show the opposite. Since regional monsoonal flow and strength is dictated by the regional topography, moisture flux, and heat and moisture exchange via land surface interactions, one must consider how all these inputs may change the seasonal δD values shown in **figure 1**.

Since the strength of the regions' monsoon events is linked to the intensity of rainfall, the variation in δD values as a function of rainfall rates (**figure 2**) during the regional wet seasons gives initial insight into monsoonal effects of isotopic fractionation during condensation for each region. This 'amount effect' (Dansgaard, 1964) of increasing isotopic depletion in precipitation with increasing precipitation rates in monsoonal regions has been statistically documented in Andean and Himalayan snow packs (Wushiki, 1977; Grootes, 1989), yet the physics underlying the process is not currently constrained by airborne δD measurements. The figure shows that while the Amazon, N. Australian, Asian Monsoon, and Congo regions' monsoon seasons show decreasing δD values with increasing precipitation rates (slopes of -3 , -9 , -3 , and -3 ‰/mm/day, respectively), the SW United States region does not (slope of 0 ‰/mm/day). The amount effect appears as a fairly robust component causing deuterium depletion of water vapor during the tropical continents' rainy seasons and can be shown to be the dominant feature producing seasonal δD differences in the Amazon, Congo, and Asian Monsoon regions; however, it does not explain the unique seasonal differences in δD values for the N. Australian or SW United

States regions (**figure 1**). Instead, the TES δD measurements indicate that the δD seasonal differences over N. Australia and the SW United States are linked to inter-seasonal variations in moist convection and moisture advection.

A comparison of models in the Stable Water Isotope Intercomparison Group (SWING) has shown that while regional precipitation and atmospheric vapor amounts are fairly well modeled, the failure of these models to accurately represent isotopic variations, like those of the TES δD measurements, suggests they do so for the wrong reasons. By looking at the relationships between the isotope measurements and the various meteorological parameters, validation requirements for isotope-enabled GCMs are established.

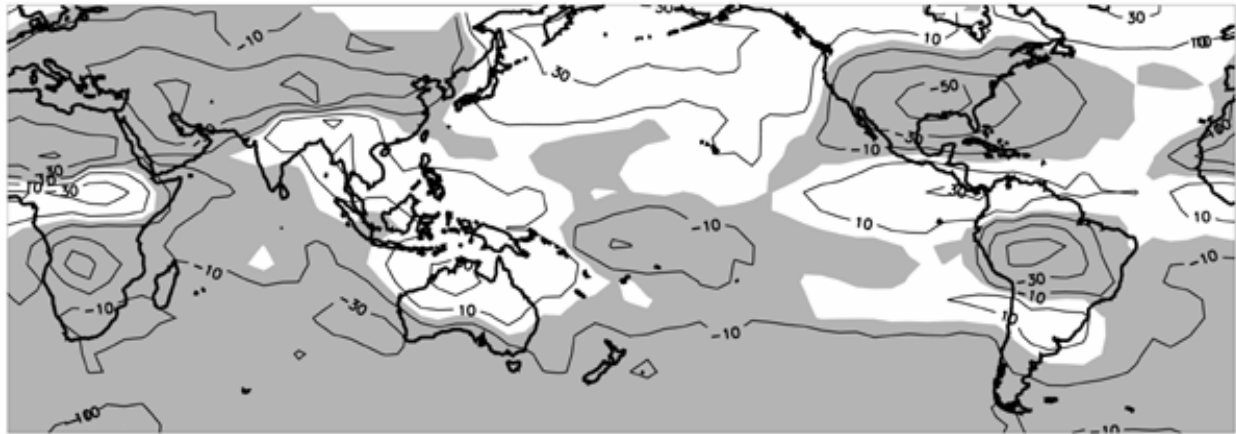


Figure 1: DJF-JJA δD values (‰) for the atmospheric level 300-850mb derived from TES retrievals during 2004-2006. Shaded areas indicate negative values, while solid line contour intervals are 20%.

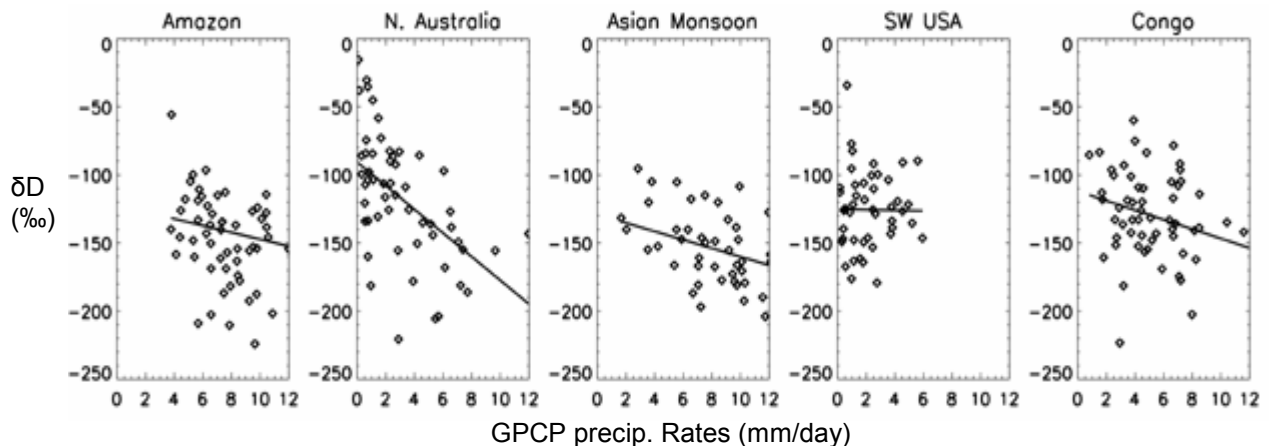


Figure 2: Daily averaged wet season (DJF for SH, JJA for NH) TES δD (‰) as a function of Global Precipitation Climatology Project (GPCP) precipitation rates (mm/day) for five convectively active regions around the globe.

References

- 1) Dansgaard, W. (1964): Stable isotopes in precipitation. *Tellus* **16**, 436-468
- 2) Gat, J.R. (1996): Oxygen and hydrogen isotopes in the hydrologic cycle. *Ann. Rev. Earth Planet Sci.* **24**, 225-262
- 3) Grootes, P. M., M. Stuiver, L.G. Thompson, and E. Mosley-Thompson (1989): Oxygen Isotope Changes in Tropical Ice, Quelccaya, Peru. *Journal of Geophysical Research* **94**, 1187-1194.
- 4) Werner, M., et al., 2004: SWING - The Stable Water Isotope Intercomparison Group: Eos Trans. AGU, 85 Fall Meet. Assem. Suppl., Abstract C51B-1034
- 5) Wushiki, H. (1977): Deuterium content in the Himalayan precipitation at Khumbu District, observed in 1974/1975. SEPPY0 (*Journal of the Japanese Society of snow and ice*) **39** (Special Issue), 50-56.

Marine Wind Analysis with the Benefit of Radarsat-1 Synthetic Aperture Radar Data

Richard Danielson¹, Michael Dowd², and Harold Ritchie^{1,3}

¹Oceanography, Dalhousie University, Halifax, Nova Scotia

²Mathematics and Statistics, Dalhousie University, Halifax, Nova Scotia

³Environment Canada, Dartmouth, Nova Scotia

It is well known that remote sensing can lead to improved marine forecasts in regions that are otherwise poorly observed. Atmospheric upper level and boundary layer processes are often manifested by coherent wind structures at the surface with various spatial scales above a few meters. Although the footprint of these structures can be observed using, for example, space-based scatterometers (with O[10-km] resolution) and synthetic aperture radars (with O[10-m] resolution), this type of information is often underutilized when analyzing marine winds.

The objective of this work is to estimate the relative errors in synthetic aperture radar (SAR) wind information, with the expectation that data assimilation tests will subsequently explore their impact on forecasts. A nonlinear regression approach is employed in which these errors are postulated. These postulates are then used to construct analyses with minimum error variance from SAR acquisitions and Global Environmental Multiscale (GEM) model forecasts. Two SAR–wind relationships are considered here. The first is the European Remote Sensing (ERS) C-Band model with the Radarsat-1 polarization correction of Vachon and Dobson (2000) (and we denote the composite function by \mathbf{c} below). This provides an estimate of SAR backscatter given wind speed and direction. The second is based on the proposition that SAR acquisitions resolve coherent wind streak patterns at O[100-m] scales that can be used to determine wind direction. This 180°-ambiguous wind direction (which we multiply by two, modulus 360°, and denote by a unit vector \mathbf{d}_s below) is derived from the local SAR backscatter gradient following Koch (2004).

Errors in SAR and GEM data are expected to be indicative of the proper composition of a surface wind analysis in the least-squares sense. If \mathbf{x} is an estimate of the true wind field, the standard regression form for the SAR and GEM data and their errors (\mathbf{e}) is

$$\begin{pmatrix} \mathbf{y}_s \\ \mathbf{d}_s \\ \mathbf{x}_g \end{pmatrix} = \begin{pmatrix} \mathbf{c}(\mathbf{x}) \\ \mathbf{d}(\mathbf{x}) \\ \mathbf{x} \end{pmatrix} + \begin{pmatrix} \mathbf{e}_s \\ \mathbf{e}_d \\ \mathbf{e}_g \end{pmatrix}. \quad (1)$$

Here, each term is a column matrix of dimension $5N$ (for a SAR scene with N valid observations). The lhs term contains the SAR radar cross section (\mathbf{y}_s), the two components of the unit vector pointing at twice the angle of the observed wind streaks (\mathbf{d}_s), and the two components of the GEM model winds (\mathbf{x}_g). The first term on the rhs involves \mathbf{d} , which provides a unit vector at each analysis location that points at twice the angle of the estimated true wind vector. The second term on the rhs contains errors in the SAR backscatter (\mathbf{e}_s), in the use of SAR gradients to estimate wind direction (\mathbf{e}_d), and in the GEM wind components (\mathbf{e}_g). We define vectors by their cross-track (u) and along-track (v) components and express radar cross section in decibels.

An estimate of the true wind field with minimum error variance is obtained by minimization of a cost function J . Given the above equation, the corresponding cost function is

$$J = \|\mathbf{y}_s - \mathbf{c}(\mathbf{x})\|_{\mathbf{R}}^2 + \|\mathbf{d}_s - \mathbf{d}(\mathbf{x})\|_{\mathbf{D}}^2 + \|\mathbf{x} - \mathbf{x}_g\|_{\mathbf{B}}^2. \quad (2)$$

The analysis \mathbf{x} that minimizes J is thus a function of the postulated SAR backscatter, SAR gradient, and GEM error covariance matrices (\mathbf{R} , \mathbf{D} , and \mathbf{B} , respectively). We treat the GEM wind errors

Corresponding author email: rick.danielson@phys.ocean.dal.ca

as homogeneous and isotropic streamfunction and velocity potential errors, following Daley (1991), with fixed along- and cross-flow variance of $5 \text{ m}^2 \text{ s}^{-2}$ (the diagonal elements of \mathbf{B}) and spatial covariance that decays exponentially with a length scale of 350 km. For the SAR acquisition illustrated in Fig. 1, we postulate that the SAR backscatter error variance is 1.5% of the SAR backscatter itself (Portabella et al. 2002) and the covariance decays with a length scale of 15 km. The directional errors are simply assigned a variance of 0.1, which corresponds to placing high confidence in the gradient calculation as an indication of wind direction.

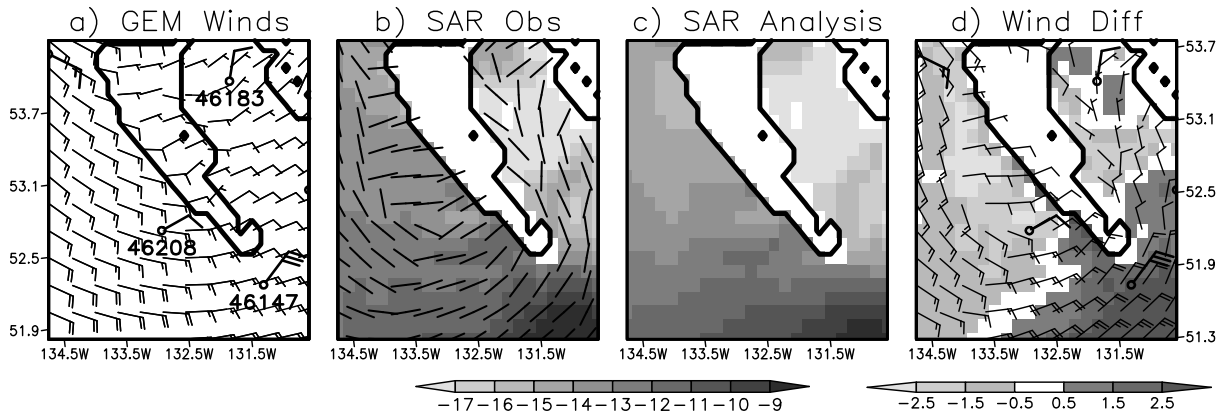


Figure 1: Surface wind analysis near the Queen Charlotte Islands on December 12, 2004: a) GEM model winds with four buoy observations, b) SAR backscatter with its range dependence removed and wind streak direction obtained following Koch (2004), c) the retrieved backscatter $\mathbf{c}(\mathbf{x})$ that minimizes J , and d) the corresponding wind analysis (barbs) along with GEM minus analysis wind speed differences (shaded).

Buoy observations that are vertically adjusted to the 10-m reference level (Walmsley 1988) and available within 30 minutes of Radarsat overpass have been used to tune our SAR error covariances. Figure 1b reveals the wind directions obtained from gradients in SAR backscatter at 400-m resolution are quite consistent with the buoys, which implies that the former should be weighted strongly. The resulting wind speeds also more consistent with buoys than the GEM forecast: the analyzed winds are slower than the GEM winds to the west and faster to the southeast.

Further comparison of analyses and buoy observations (not shown) suggests that the SAR error variance may be about 1.5% of SAR backscatter and have a length scale of about 15 km, which is much less than the resolution of scatterometer data (which is not considered to have spatial error covariance). One caveat here is that our postulated SAR errors are predicated on the assumption that the buoy observations can be used as a reference. Although this is expected to yield a good preliminary error estimate, buoy errors may limit their accuracy (Stoffelen 1998).

References

- Daley, R., 1991: *Atmospheric Data Analysis*. Cambridge University Press, New York, New York, 457 pp.
- Koch, W., 2004: Directional analysis of SAR images aiming at wind direction. *IEEE Trans. Geosci. Remote Sens.*, **42**, doi:10.1109/TGRS.2003.818811.
- Portabella, M., A. Stoffelen, and J. A. Johannessen, 2002: Toward an optimal inversion method for synthetic aperture radar wind retrieval. *J. Geophys. Res.*, **107**, doi:10.1029/2001JC000925.
- Stoffelen, A., 1998: Toward the true near-surface wind speed: Error modeling and calibration using triple collocation. *J. Geophys. Res.*, **103**, 7755–7766.
- Vachon, P. W., and F. W. Dobson, 2000: Wind retrieval from RADARSAT SAR images: Selection of a suitable C-band HH polarization wind retrieval model. *Can. J. Remote Sens.*, **26**, 306–313.
- Walmsley, J. L., 1988: On theoretical wind speed and temperature profiles over the sea with applications to data from Sable Island, Nova Scotia. *Atmos.–Ocean*, **26**, 203–233.

Tokyo Radar Wind Data Assimilation with the JMA Meso 4D-VAR¹

Yoshihiro Ishikawa

Numerical Prediction Division, Japan Meteorological Agency
1-3-4 Otemachi, Chiyoda-ku, Tokyo 100-8122, Japan

E-mail: ishikawa@met.kishou.go.jp

The Japan Meteorological Agency (JMA) started the use of radial velocity data (Vr) of Tokyo radar with the JMA operational mesoscale 4D-VAR analysis on December 11, 2006. Precision of a precipitation forecast improved from information of wind of rainfall area in an initial condition of the mesoscale numerical weather prediction (NWP).

To estimate the impact of assimilating the Vr of Tokyo radar in NWP routine, three-hourly forecast-analysis cycle was performed without and with the Vr of Tokyo radar in the period during 8-17 June 2006. In this period, 15-hour forecasts were made eight times a day at 00, 03, 06, 09, 12, 15, 18, and 21 UTC.

Fig.1. shows the Vr of Tokyo radar has significantly positive impacts on the precipitation forecasts.

Fig.2. shows a case of heavy rain in the experiment period. Fig.2a. and 2c. show, respectively, the forecast of 3-hour precipitation amount starting from the mesoscale 4D-Var analysis without and with the Vr of Tokyo radar. Fig.2b. shows the corresponding observation for the Radar-Raingauge Analyzed Precipitation from conventional weather radar. Without the Vr of Tokyo radar, the amount of the precipitation forecast in the rainfall area of North Kanto which is located in the down stream area of Tokyo radar (indicated by broken line's circle) was much smaller than that of the observation. By assimilating the Vr of Tokyo radar (Fig.2c.), more precipitation is predicted and the precipitation pattern is closer to the observation.

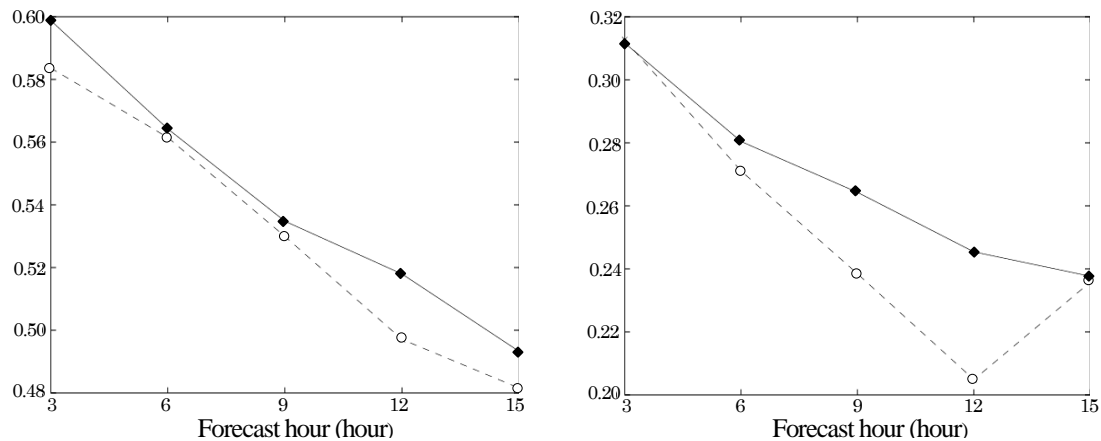


Fig.1 Threat score of 3-hour accumulated precipitation forecast over Japan starting from analysis with the Vr of Tokyo radar (solid line) and without them (broken line) for the period from 8 to 17 June, 2006. Threshold values are 1 mm (left) and 10 mm (right) with a horizontal resolution of 10 km.

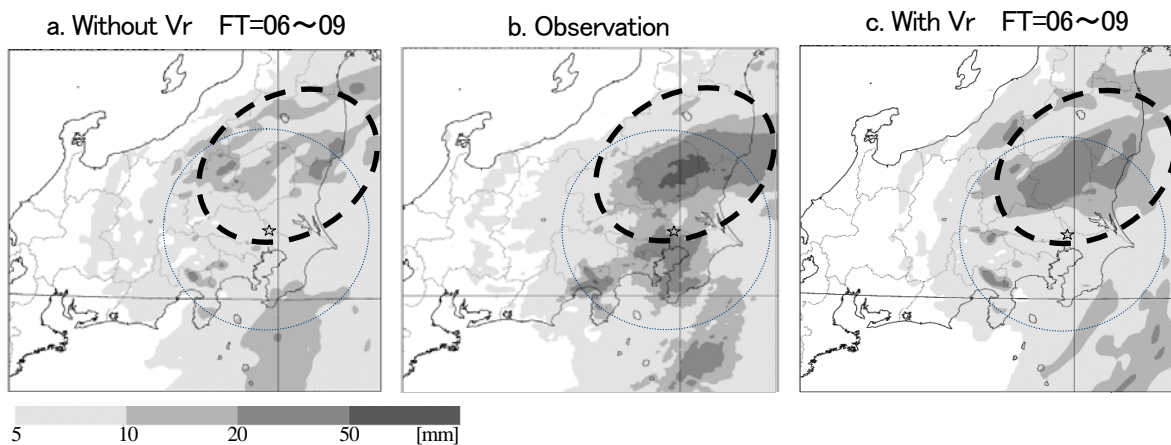


Fig.2 Verification of 3-hour accumulated precipitation forecast starting from initial conditions at 15UTC 15 June 2006. Left: the 06-09 forecasts starting from the 4D-Var analysis without the Vr of Tokyo radar. Center: the Radar-Raingauge Analyzed Precipitation. Right: the 06-09 forecasts starting from the 4D-Var analysis with Vr.

¹ The JMA Meso 4D-VAR is mesoscale analysis system to prepare initial condition for the JMA Meso Scale Model (MSM).

Applying a local ensemble transform Kalman filter to the JMA global model

Takemasa Miyoshi*[†] and Yoshiaki Sato*

*Numerical Prediction Division, Japan Meteorological Agency

In the 2006 issue of the WGNE Blue Book, Miyoshi and Yamane (2006) reported their successful implementation of the local ensemble transform Kalman filter (LETKF, Hunt 2005) with the AFES model (AGCM for the Earth Simulator). They made further comprehensive investigations; the results are now in press in Monthly Weather Review (Miyoshi and Yamane 2007). In the meantime, based on the investigations on the Earth Simulator, LETKF has been developed with the JMA's global model (GSM) at a TL159/L40 resolution, which is the same version as the one used in the operational ensemble prediction system (EPS). In this short report, we briefly overview our preliminary results with the GSM-LETKF.

First, 20-member LETKF has been performed to ensure that the system works appropriately (Miyoshi and Sato 2007, hereafter "MS07"). MS07 investigated impacts by assimilating satellite radiances. Fig. 1 shows the results by MS07, where we see clear advantages of the satellite radiance assimilation. Here, the parameter values are fixed with the 21x21x13 local patch (about 1000-km radius), 5-grid (about 500-km) horizontal and 3-grid vertical Gaussian localization, and 10 % spread inflation.

Then, the ensemble size has been increased to be 50 with the same parameter values. Figs. 2 and 3 show the results, where we see significant improvements by the larger ensemble size. Still, LETKF shows

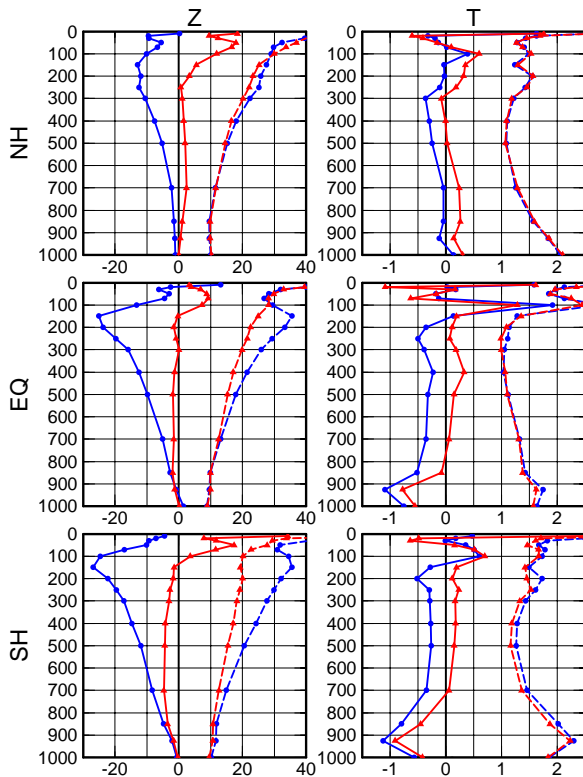


Figure 1. Analysis errors of height (m, left) and temperature (K, right) verified against radiosonde observations in each area for the cases with (red) and without (blue) satellite radiances, temporally averaged over 31 days in August 2004 (adapted from Fig. 5 of MS07). Solid and dashed lines indicate the bias and RMS errors, respectively.

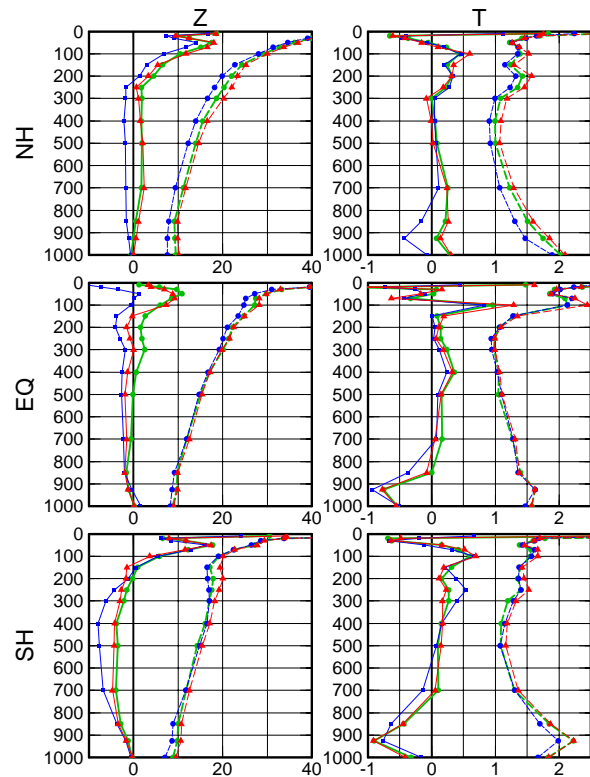


Figure 2. Similarly to Fig. 1, but for the cases of the LETKF with 20 members (red), LETKF with 50 members (green), and the operational 4D-Var (blue).

[†] Corresponding author address: Numerical Prediction Division, Japan Meteorological Agency, 1-3-4 Otemachi, Chiyoda-ku, Tokyo 100-8122, Japan. E-mail: miyoshi@naps.kishou.go.jp

generally larger errors than the operational 4D-Var (Kadowaki 2005).

After the above investigations, Miyoshi et al. (2007) developed a new version of the LETKF that does not use local patches. Without local patches, there is no need to specify the local patch size, thus the number of the localization tuning parameters are reduced. Moreover, it solves the discontinuity problem caused by the local patch near the Poles where the physical distances between successive grid points are short. The new algorithm has been applied to the GSM-LETKF. Furthermore, we apply vertical localization linear with the log-p coordinate, which is physically more meaningful. So far, the vertical localization was applied linearly with the model coordinate; in the lower troposphere where the model has a denser resolution, the vertical localization has been too narrow.

With the above upgrades, we obtained further improvements. Fig. 4 shows forecast verification scores. The blue curve shows results by the LETKF without local patches, but with the same parameters (500-km horizontal and 3-grid vertical localization with 10 % spread inflation). Red curve shows the latest results with tuned parameters (500-km horizontal and 0.5-hPa vertical localization with 30 % spread inflation), which appears to be much closer to the operational 4D-Var. We are expecting further improvements by refining the parameters and increasing the ensemble size up to 100.

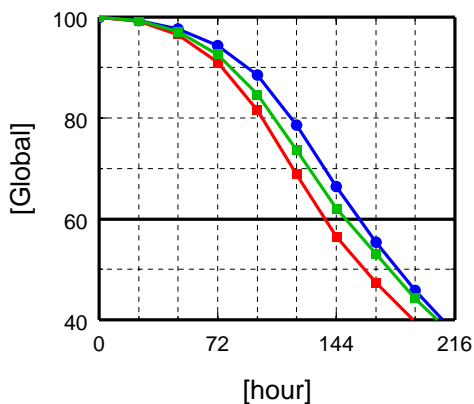


Figure 3. 9-day forecast anomaly correlations (%) of 500 hPa height averaged over 31 days in August, 2004, for the cases of the LETKF with 20 members (red), LETKF with 50 members (green), and operational 4D-Var (blue).

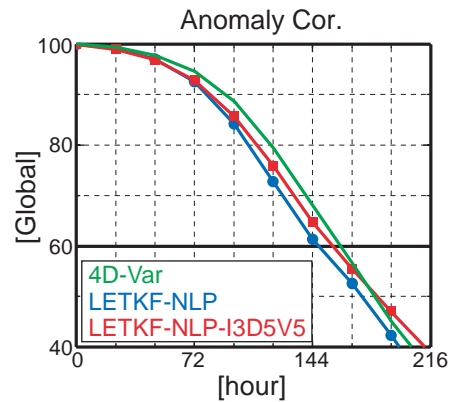


Figure 4. Similarly to Fig. 3, but for the LETKF without local patches and a different sample period (August 1-15, 2004). Blue and red lines indicate 50-member LETKF without local patches with the original and tuned parameters, respectively. Green line indicates the operational 4D-Var.

Acknowledgements

We thank Prof. Eugenia Kalnay, Drs. Shozo Yamane, Takeshi Enomoto, and Jeff Whitaker for fruitful discussions.

References

- Hunt, B. R., 2005: Efficient Data Assimilation for Spatiotemporal Chaos: a Local Ensemble Transform Kalman Filter. arXiv:physics/0511236v1, 25pp.
- Kadowaki, T, 2005: A 4-Dimensional Variational Assimilation System for the JMA Global Spectrum Model. *CAS/JAC WGNE Research Activities in Atmospheric and Oceanic Modelling*, **34**, 1-17.
- Miyoshi, T. and S. Yamane, 2006: Local ensemble transform Kalman filtering with an AGCM at a T159/L48 resolution. *CAS/JAC WGNE Research Activities in Atmospheric and Oceanic Modelling*, **35**, 1-19.
- Miyoshi, T. and S. Yamane, 2007: Local ensemble transform Kalman filtering with an AGCM at a T159/L48 resolution. *Mon. Wea. Rev.*, in press.
- Miyoshi, T. and Y. Sato, 2007: Assimilating Satellite Radiances with a Local Ensemble Transform Kalman Filter (LETKF) Applied to the JMA Global Model (GSM). *SOLA*, in press.
- Miyoshi, T., S. Yamane, and T. Enomoto, 2007: Localizing the error covariance by physical distances within a local ensemble transform Kalman filter. in preparation.

Applying a local ensemble transform Kalman filter to the JMA nonhydrostatic model

Takemasa Miyoshi*[†] and Kohei Aranami*

*Numerical Prediction Division, Japan Meteorological Agency

In the 2006 issue of the WGNE Blue Book, Miyoshi and Yamane (2006) reported their successful implementation of the local ensemble transform Kalman filter (LETKF, Hunt 2005) with the AFES model (AGCM for the Earth Simulator). They made further comprehensive investigations; the results are now in press in *Monthly Weather Review* (Miyoshi and Yamane 2007). In the meantime, based on the investigations on the Earth Simulator, LETKF has been developed with the JMA's nonhydrostatic mesoscale model (NHM). Miyoshi and Aranami (2006, hereafter "MA06") published results of perfect model twin experiments with the NHM-LETKF. In this short report, we briefly overview our preliminary results with real observations.

After the successful investigations by MA06, real observations used in JMA's operational mesoscale analysis are assimilated with the NHM-LETKF. The model domain is chosen to be the same as the JMA operational mesoscale system (about 3600km x 2900km). The resolution is reduced to be 20-km grid spacing with 181x145x50 grid points, instead of the operational 5-km grid spacing which requires 16 times more grid points. The model parameters and physical processes of the 20-km NHM are chosen to be essentially the same as the operational settings. Differences are found in the orography, land-surface, finite-differencing time, and buffer area near the boundaries, all of which are minimum required changes by the resolution difference. The ensemble size is chosen to be 20. The data assimilation cycle begins on June 25, 2004.

Figure 1 shows 6-hour forecast fields (i.e., first guess) of the NHM-LETKF and JMA operational mesoscale NWP systems. The operational mesoscale NWP system as of June and July 2004 was not NHM but a hydrostatic spectral model with 10-km grid spacing, thus it is not straightforward to compare them precisely. Although NHM-LETKF indicates a little higher pressure, the position of the low pressure system and the precipitation pattern show good agreements.

Figure 2 shows analysis ensemble spreads after the first analysis step and a few week cycle processes. Since a large number of observations are available over Japan, the area with small spreads indicates the shape of Japan after the first analysis step. Due to the fixed boundary conditions for all ensemble members, spreads are artificially small near the boundaries, especially about 20 grids (400 km) which corresponds to the damping area. Still, we see large spreads beyond 7 m/s in the region; the errors are actually growing and not damped by the fixed boundaries. The ensemble spreads vary dynamically to show flow-dependent behaviors. The stable LETKF performance would explain that the error growth inside the region is not significantly affected by the fixed boundary conditions.

Although it is difficult to compare the analysis accuracy, the NHM-LETKF appears to generate reasonable analysis. Miyoshi et al. (2007) developed a new version of the LETKF that does not use local patches, which requires less computational time and generates better analysis without discontinuities at the edges of local patches. Future plans include applying the new version without local patches, as well as further investigations of the verifications and ensemble forecast experiments.

[†] Corresponding author address: Numerical Prediction Division, Japan Meteorological Agency, 1-3-4 Otemachi, Chiyoda-ku, Tokyo 100-8122, Japan. E-mail: miyoshi@naps.kishou.go.jp

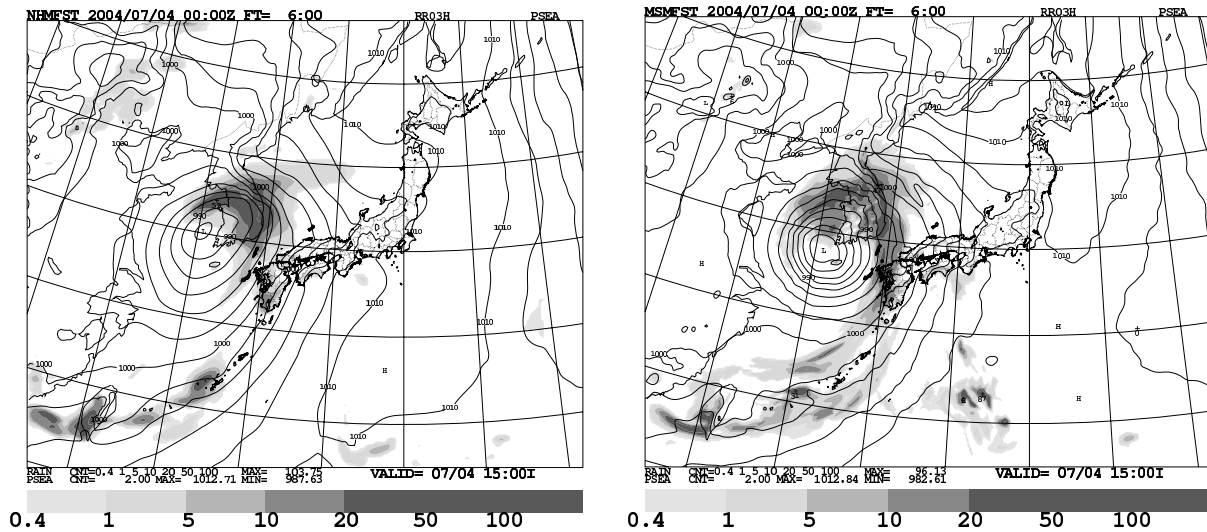


Figure 1. 3-hour accumulated precipitation (mm, shades) and sea-level pressure (contour) of NHM-LETKF 6-hour forecast ensemble mean (left) and JMA operational mesoscale 6-hour forecast (right) valid on 06Z July 4, 2004.

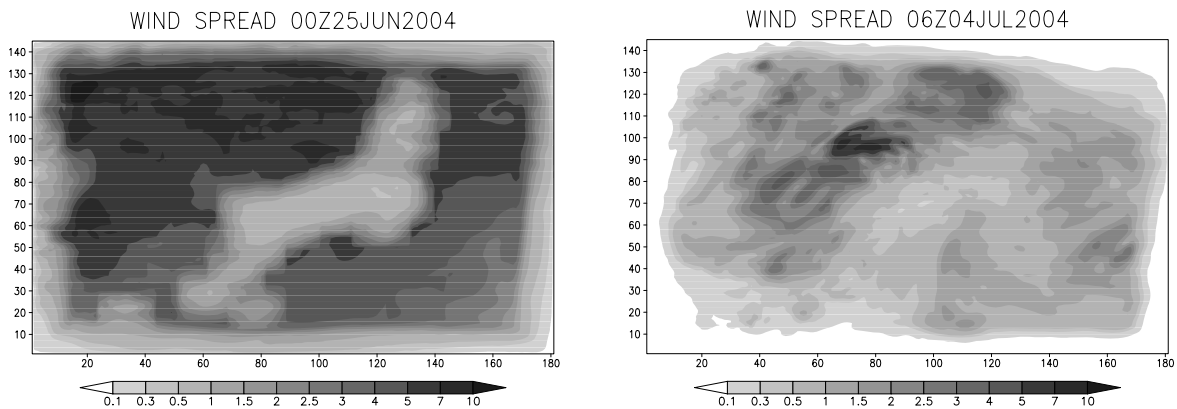


Figure 2. Horizontal pattern of the analysis ensemble spreads of wind speed (m/s) at the 21st vertical level (about 4000 meters high), after first analysis step (00Z June 25, 2004, left) and a few week cycle processes (06Z July 4, 2004, right). Horizontal and vertical axes indicate grid numbers.

Acknowledgements

We thank Prof. Eugenia Kalnay for fruitful discussions.

References

- Hunt, B. R., 2005: Efficient Data Assimilation for Spatiotemporal Chaos: a Local Ensemble Transform Kalman Filter. arXiv:physics/0511236v1, 25pp.
- Miyoshi, T. and S. Yamane, 2006: Local ensemble transform Kalman filtering with an AGCM at a T159/L48 resolution. *CAS/JAC WGNE Research Activities in Atmospheric and Oceanic Modelling*, **35**, 1-19.
- Miyoshi, T. and S. Yamane, 2007: Local ensemble transform Kalman filtering with an AGCM at a T159/L48 resolution. *Mon. Wea. Rev.*, in press.
- Miyoshi, T. and K. Aranami, 2006: Applying a Four- dimensional Local Ensemble Transform Kalman Filter (4D-LETKF) to the JMA Nonhydrostatic Model (NHM), *SOLA*, **2**, 128-131.
- Miyoshi, T., S. Yamane, and T. Enomoto, 2007: Localizing the error covariance by physical distances within a local ensemble transform Kalman filter. in preparation.

Improvement of ATOVS radiance assimilation

Kozo Okamoto

Numerical Prediction Division, Japan Meteorological Agency

1-3-4 Otemachi, Chiyoda-ku, Tokyo 100-8122, JAPAN

okamoto@naps.kishou.go.jp

JMA has been assimilating radiances of AMSU-A/B from NOAA15-17 and Aqua satellites in the global data assimilation system. In August 2006, several changes were made in ATOVS pre-processings such as improving QC, recalculating scan bias correction, and modifying AMSU-A observation errors assigned. The QC improvement includes update of an algorithm to derive total column cloud liquid water (TCCLW) used for detecting cloud/rain-affected radiances and correcting air-mass dependent observation biases, stricter gross-error QC, adding rain detection based on TCCLW, removal of edge scans and revision of channel selection. Among them, observation error modification had the largest impacts on NWP performance. The details of this modification can be found in Okamoto et al. (2006).

Cycle experiments were carried out for 20 July through 9 September 2004 (EXP1) and 20 December 2004 through 9 February 2005 (EXP2) to assess these changes. With the new ATOVS pre-processings, the fit of temperature analysis against radiosondes became better in the Tropics and Southern Hemisphere although worse in the stratosphere of the Northern Hemisphere. The forecast impacts for the 850 hPa temperature and 500 hPa geopotential height are positive in the Tropics and Southern Hemisphere while neutral in the Northern Hemisphere. This is shown in Fig.1 in terms of improvement rate of root mean square forecast error (RMSFE) defined by $[(\text{RMSFE}_{\text{cnt1}} - \text{RMSFE}_{\text{test}}) / \text{RMSFE}_{\text{cnt1}}]$. Especially there are obvious positive impacts in short-range forecast in the Southern Hemisphere. Typhoon track forecast errors are clearly reduced at the forecasts of 30-h and hereafter (Fig.2).

References

Okamoto, K. H. Owada, Y. Sato, and T. Ishibashi, 2006: Use of satellite radiances in the global assimilation system at JMA. in Technical Proceedings of the 15th International ATOVS Study Conference, Matatea, Italy, 4-10 October 2006.

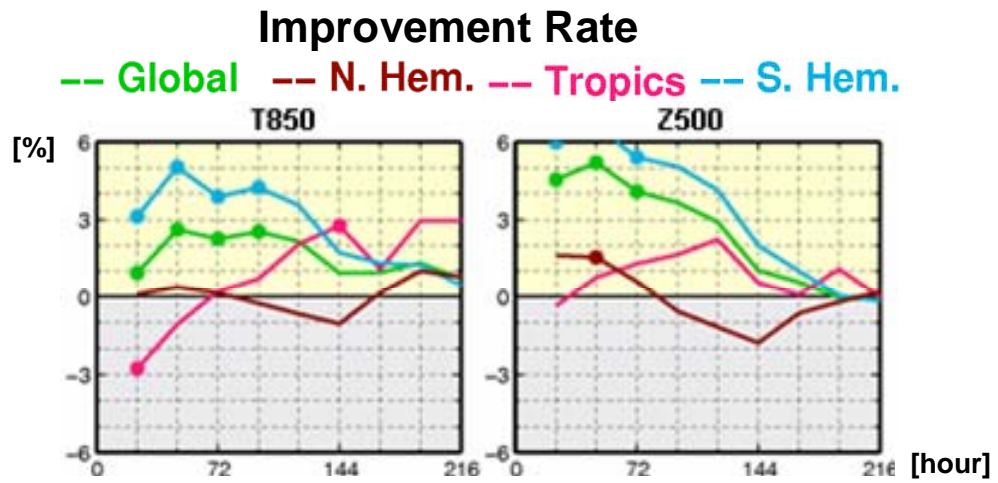


Fig.1: Improvement rate (see text) of forecast error of 850 hPa temperature and 500 hPa geopotential height as a function of forecast hours up to 216 hours for the experiment of EXP1. Dots on these score lines represent statistical significance.

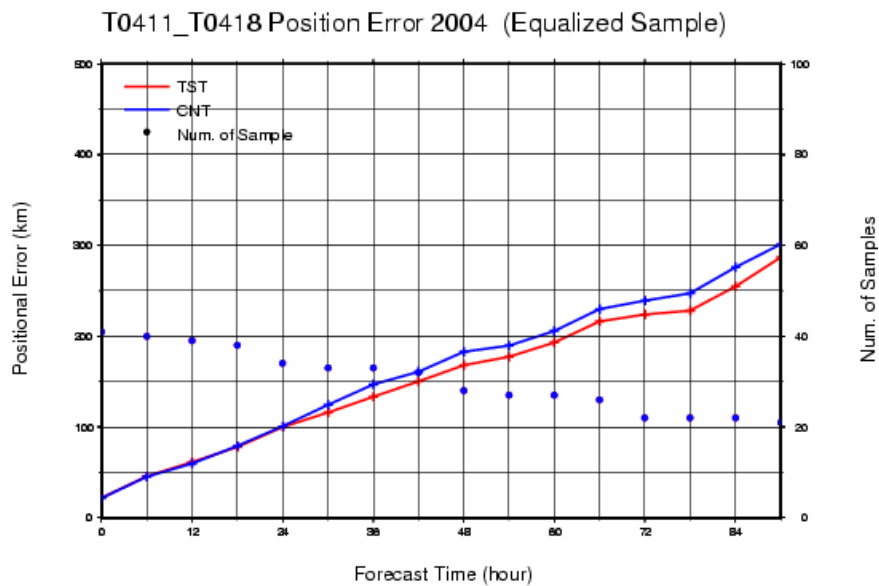


Fig.2: Typhoon track forecast errors of the run with improved ATOVS processing (red line) and old processing (blue line) in EXP1. The number of cases used in this statistics is dotted with the scale at the right.

Assimilation of space based GPS occultation data for JMA GSM

Eiji OZAWA⁽¹⁾, Yoshiaki SATO⁽¹⁾, Hideo TADA⁽²⁾ and Yuichi AOYAMA⁽³⁾

(1) Numerical Prediction Division, Japan Meteorological Agency¹

(2) Forecast Division, Japan Meteorological Agency

(3) National Institute of Polar Research

1 Introduction

A data assimilation (DA) system of space-based GPS radio occultation data has been developed for JMA Global Spectral Model (GSM). This scheme will be implemented to GSM soon. The GPS data have high potential to improve the initial field of the GSM because of their global distribution with high vertical resolution. As of February 2007, we receive CHAMP (CHALLENGING Mini-satellite Payload) data from GFZ² through the Internet (Wickert et al. 2000).

2 Methods

There are various data forms for GPS data assimilation, such as assimilating excess path length, bending angle, refractivity, and retrieved temperature and specific humidity. Among them, refractivity data assimilation was examined for operational use at JMA, because it is one of the most cost-effective methods. The data were used with height from 5km to 35km where small biases were found. A procedure to correct observation biases is based on a linear regression approach and their regression coefficients are estimated by Kalman filter in every analysis. The predictors for the bias correction are latitude, height, and refractivity. Fig.1 shows cross section of observation innovation (O-B), and Fig.2 shows the amount of bias correction. Observation errors were determined as a function of height in five latitudinal bands independently.

3 Assimilation experiments

Observation system experiment for the GPS refractivity data (TEST) was conducted for August 2004 and January 2005, and it was compared with the control experiment (CNTL) with the global 4D-Var analysis system to assess the impacts of GPS refractivity assimilation. Tables 1 and 2 show mean improvement rates³ of RMS forecast errors against initial field for the August experiment and January experiment, respectively. They show positive impacts by assimilating CHAMP data in almost all areas. Typhoon track forecast errors are also slightly reduced after FT=60 (not shown).

4 Acknowledgements

We acknowledge GFZ for providing the CHAMP data.

¹ Otemachi, Chiyoda-ku, Tokyo 100-8122, Japan E-mail: e-ozawa@naps.kishou.go.jp

² GeoForschungsZentrum Potsdam

³ Mean improvement rate = $\sum_{i=1}^9 \frac{-(RMS_{test} - RMS_{cntl})}{RMS_{cntl}} \times 100$

i corresponds to nine forecast hours of 24,48,72,96,120,144,168,192 and 216.

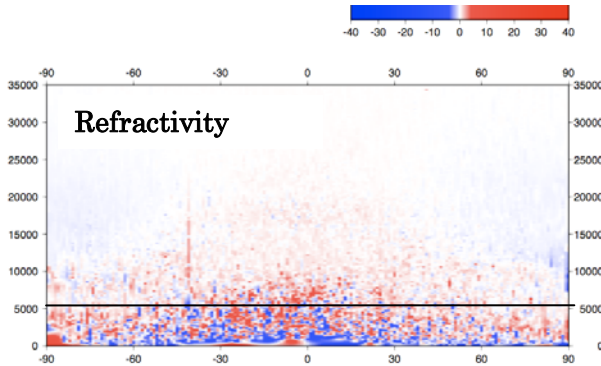


Fig.1 Cross section of observation innovation (O-B) before bias correction. Vertical axis means altitude (km) and horizontal axis means latitude. An investigation period is on July 20 to September 9, 2004.

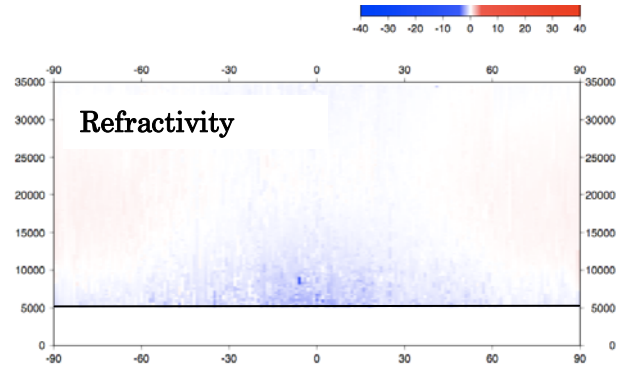


Fig.2 Amount of bias correction of refractivity. The data were used with height from 5km to 35km.

Table 1 August experiment : Improvement rate of RMS forecast errors against initial fields in the various elements in the August experiment. Yellow means improvement more than 0.1%, white means neutral and gray means deterioration more than 0.1%.

Table 2 January experiment : Same as Table 1, but for January.

Global				Northern Hemisphere				Global				Northern Hemisphere			
GL	Z	T	Wind	NH	Z	T	Wind	GL	Z	T	Wind	NH	Z	T	Wind
300	0.68	0.27	0.29	300	1.00	-0.01	0.36	300	0.43	0.12	0.13	300	0.64	0.09	0.27
500	0.84	0.33	0.42	500	1.02	0.55	0.34	500	0.42	0.43	0.20	500	0.54	0.61	0.34
850	0.61	0.34	0.32	850	0.69	0.60	0.24	850	0.34	0.26	0.10	850	0.58	0.53	0.26
Psea	0.48			Psea	0.44			Psea	0.36			Psea	0.61		
Tropics				Southern Hemisphere				Tropics				Southern Hemisphere			
TR	Z	T	Wind	SH	Z	T	Wind	TR	Z	T	Wind	SH	Z	T	Wind
300	0.23	0.76	0.15	300	0.55	0.38	0.27	300	-0.25	0.44	0.14	300	0.28	0.11	0.01
500	0.19	0.31	0.41	500	0.77	0.24	0.45	500	0.04	0.41	0.17	500	0.35	0.18	0.06
850	0.02	0.65	0.05	850	0.59	0.18	0.44	850	-0.01	0.08	0.07	850	0.20	-0.05	-0.03
Psea	0.04			Psea	0.48			Psea	0.14			Psea	0.15		

Reference

Wickert, J., C. Reigber, G. Beyerle, R. König, C. Marquardt, T. Schmidt, L. Grunwaldt, R. Galas, T. K. Meehan, W. G. Melbourne, and K. Hoche, 2000: Atmosphere sounding by GPS radio occultation: First results from CHAMP. *Geophys. Res.*, **28**, 3263-3266.

Introduction of spaceborne microwave imager radiance data into the JMA global data assimilation system

Yoshiaki Sato

Numerical Prediction Division, Japan Meteorological Agency

1-3-4 Otemachi, Chiyoda-ku, Tokyo 100-8122, JAPAN

E-mail: y-sato@met.kishou.go.jp

The brightness temperature (TB) data from spaceborne microwave imagers, such as DMSP/SSM/I, TRMM/TMI, and Aqua/AMSR-E, have been introduced into the JMA global data assimilation (DA) system in May 2006 with variational bias correction technique (VarBC, Derber and Wu 1998).

Those data are used over the clear sky or thin cloudy ocean with sea surface temperature (SST) higher than 5 degree Celsius. Thick cloudy and rainy areas are masked by using TB based parameters, such as the ratio of horizontal polarized TB to vertical one. The data are thinned by 200 x 200 km grid box for each time slot to neglect the spatial error correlation. The assimilated channels are vertical polarized channels of SSM/I and corresponding channels of TMI and AMSR-E. The channels and observation error settings are summarized in Table 1. The observation errors are set to 4 times the errors estimated in the preparatory analysis. Figure 1 shows an example of the assimilated data distribution.

Radiative transfer model RTTOV7 (Saunders et al 2002) is employed for TB calculation. Bias of the observations is corrected by using VarBC. Bias correction predictors for the VarBC are total column precipitable water, SST, square of SST, surface wind speed, secant of the satellite zenith angle, and unity (constant).

Observation system experiment with the MWR TB data (TEST) was carried out and compared with control experiment (CNTL). The study period was August 2004 and January 2005. Results of the experiment showed positive impact on the typhoon track forecast (Fig. 2). The position error against JMA best track data was reduced especially in the forecast time from 36 to 60 hour. The rainfall amount distribution of 24-hour forecast (R24) was also improved. The evaluation was made by using GPCP monthly averaged daily rainfall data (Adler et al 2003). The correlation coefficient of R24 against GPCP product in August 2004 for CNTL was 0.881 and it for TEST was 0.891. The coefficient in January 2005 for CNTL was 0.835 and it for TEST was 0.841. Figure 3 shows R24 of TEST and CNTL, and GPCP product in August 2004. The rainfall over Arabian Sea and west coast of India was much suppressed in TEST. The impact on forecasts of the 500 hPa geopotential height was almost neutral.

Table 1. Assimilated channels and the observation error settings (Unit: K).

Freq. and Pol.(H/V)	DMSP13	DMSP14	DMSP15*		TRMM		Aqua
	SSM/I				TMI		AMSR-E
19V	9.28	9.68	9.48	19V	10.00	18V	8.20
22V	14.60	15.44	15.04	21V	14.80	23V	13.80
37V	8.64	8.72	8.56	37V	8.40	36V	8.60
85V	11.28	11.24	10.92	85V	10.40	89V	11.80

*DMSP15/SSM/I data assimilation has been discontinued from Aug 2006, because of the US navy's activation of a radiation/calibration beacon.

References:

- Adler, R.F., G.J. Huffman, A. Chang, R. Ferraro, P. Xie, J. Janowiak, B. Rudolf, U. Schneider, S. Curtis, D. Bolvin, A. Gruber, J. Susskind, and P. Arkin, 2003: The Version 2 Global Precipitation Climatology Project (GPCP) Monthly Precipitation Analysis (1979-Present). *J. Hydrometeor.*, **4**, 1147-1167.
- Derber, J. C., and W. -S. Wu 1998: The use of TOVS cloud-cleared radiances in the NCEP SSI analysis system. *Mon. Wea. Rev.*, **126**, 2287-2299.
- Saunders, R., 2002: RTTOV-7 Users Guide. Eumetsat, 21pp. available from http://www.metoffice.com/research/interproj/nwpsaf/rtm/rttov7_ug.pdf

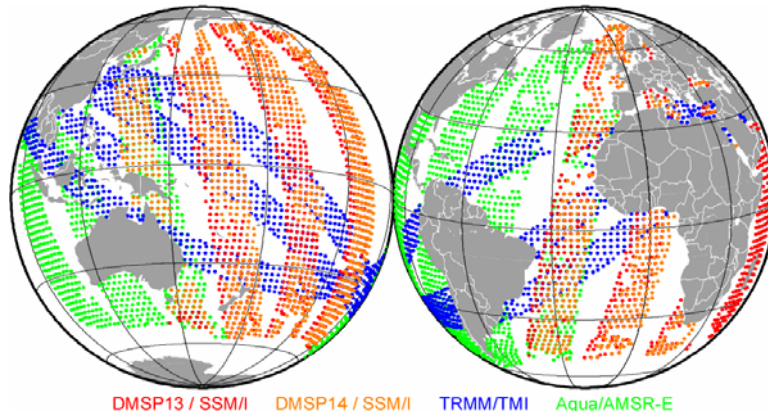


Figure 1. Sample of the assimilated data distribution in the JMA global DA system at 06UTC, 15 Nov 2006. Red symbol shows DMSP13/SSM/I, orange DMSP14/SSM/I, blue TRMM/TMI and green Aqua/AMSR-E.

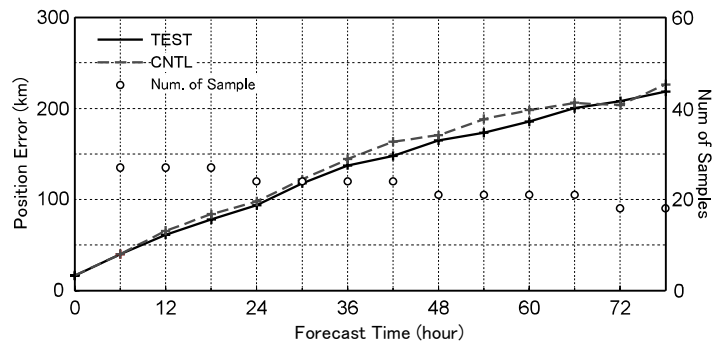


Figure 2. Time sequence of the typhoon position error against JMA best track data. Solid line shows TEST and dashed line shows CNTL

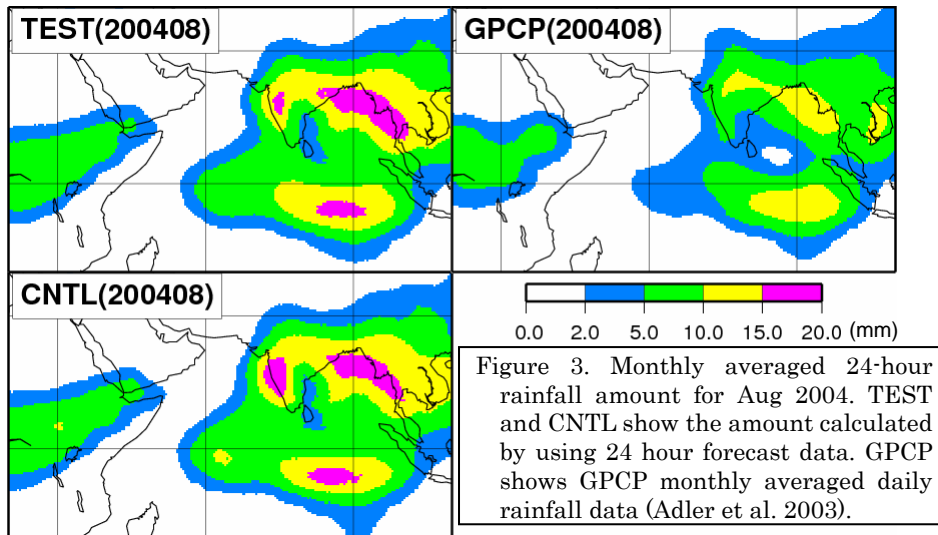


Figure 3. Monthly averaged 24-hour rainfall amount for Aug 2004. TEST and CNTL show the amount calculated by using 24 hour forecast data. GPCP shows GPCP monthly averaged daily rainfall data (Adler et al. 2003).

Introduction of variational bias correction technique into the JMA global data assimilation system

Yoshiaki Sato

Numerical Prediction Division, Japan Meteorological Agency

1-3-4 Otemachi, Chiyoda-ku, Tokyo 100-8122, JAPAN

E-mail: y-sato@met.kishou.go.jp

Variational bias correction technique (VarBC), which was originally developed at NCEP (Derber and Wu 1998), has been introduced into the JMA global data assimilation (DA) system in May 2006. The technique is an adaptive bias correction technique. In the DA system with VarBC, observation operators and control variables are extended to include bias correction procedures. The bias correction coefficients are optimized as control variables in the each analysis.

The formulation of the VarBC is based on Dee (2004). The extended control variable \mathbf{z} is defined as $\mathbf{z}^T = [\mathbf{x}^T, \boldsymbol{\beta}^T]$, where \mathbf{x} means the control variables and $\boldsymbol{\beta}$ the bias correction coefficients. Extended cost function J is defined as follows:

$$J(\mathbf{z}) = \frac{1}{2}(\mathbf{x} - \mathbf{x}^b)^T \mathbf{B}^{-1}(\mathbf{x} - \mathbf{x}^b) + \frac{1}{2}(\boldsymbol{\beta} - \boldsymbol{\beta}^b)^T \mathbf{B}_\beta^{-1}(\boldsymbol{\beta} - \boldsymbol{\beta}^b) + \frac{1}{2}(\tilde{H}(M(\mathbf{x})) - \mathbf{y}^o)^T \mathbf{R}^{-1}(\tilde{H}(M(\mathbf{x})) - \mathbf{y}^o)$$

$$\tilde{H}(M(\mathbf{x})) = H(M(\mathbf{x})) + \sum_{i=1}^n \beta_i p_i(M(\mathbf{x}^b))$$

where superscript b denotes background, \mathbf{y}^o the observations, \mathbf{B} the error covariance matrix for \mathbf{x} , \mathbf{B}_β the matrix for $\boldsymbol{\beta}$, \mathbf{R} the matrix for \mathbf{y}^o , M the time progress operator for the observation time of \mathbf{y}^o , \tilde{H} the extended observation operator to include the bias correction term, H the original observation operator, p the operator for bias correction predictors, and n the number of bias correction predictors. The optimized \mathbf{z} can be obtained by minimizing J . In this implementation, \mathbf{B}_β is defined as follows:

$$\mathbf{B}_\beta = \text{diag}(\sigma_{\beta_1}^2, \sigma_{\beta_2}^2, \dots, \sigma_{\beta_n}^2), \quad \sigma_{\beta}^2 = \begin{cases} \sigma_{obs}^2 / N_{MIN} & N < N_{MIN} \\ \sigma_{obs}^2 / (N / (\log_{10}(N / N_{MIN}) + 1)) & N \geq N_{MIN} \end{cases}, \quad N_{MIN} = 400$$

where σ_{β} denotes the background error for bias correction coefficients, σ_{obs} the observation error, and N the number of the assimilated data. N_{MIN} means a reference observation number, which was empirically defined. With this formulation, $\boldsymbol{\beta}$ changes rapidly (slowly) when N is larger (smaller) than N_{MIN} .

The technique is applied to the operationally assimilated satellite radiance data, which are NOAA/AMSU-A, NOAA/AMSU-B, Aqua/AMSU-A, DMSP/SSM/I, TRMM/TMI and Aqua/AMSR-E. The bias correction predictors for those instruments as of January 2007 are summarized in table 1.

A long term cycle analysis experiment with VarBC (TEST) was performed from April 2005 to March 2006 and compared with routine analysis before introducing VarBC (RTN). Mean error (ME) and root mean square error (RMSE) of brightness temperature (TB) departure from first-guess of AMSU-A channel 6 aboard NOAA 15 were increased from February 2006 to the beginning of March 2006 on RTN (Gray thin lines in Fig. 1). In contrast, the ME and RMSE are quite stable on TEST (Black thick lines in Fig. 1). Figure 2 shows time sequence of the bias correction coefficient on surface temperature for the TB data during the same period. The change shows the similar tendency to RMSE on RTN with several days behind. It means the VarBC effectively corrected the bias of the radiance by changing the bias correction coefficients.

Table 1. Bias correction predictors for each sensor

Instrument	Predictors
AMSU-A	Integrated weighted lapse rate, Surface temp., Total cloud liquid water, sec(SZA*), Const.
AMSU-B	Integrated weighted lapse rate, Surface temp., sec(SZA*), Const.
SSM/I	Precipitable water, SST, SST ² , Surface Wind Speed, sec(SZA*), Const.
TMI	Precipitable water, SST, SST ² , Surface Wind Speed, sec(SZA*), Const.
AMSR-E	Precipitable water, SST, SST ² , Surface Wind Speed, sec(SZA*), Const.

*SZA: satellite zenith angle

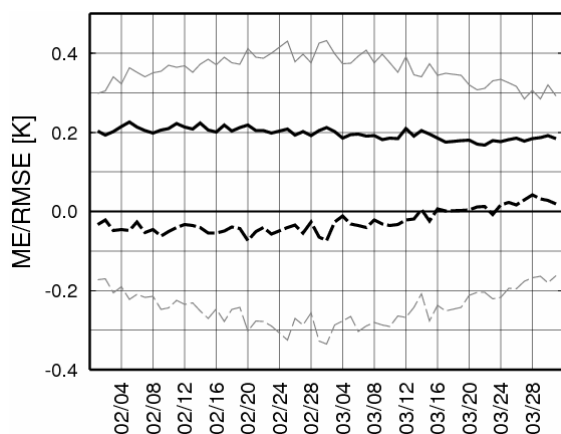


Figure 1. Time sequence of ME and RMSE of TB on channel 6 of AMSU-A aboard NOAA15 against first guess from Feb 2006 to Mar 2006. Dashed lines show ME and solid lines RMSE, gray thin lines show RTN and black thick lines TEST.

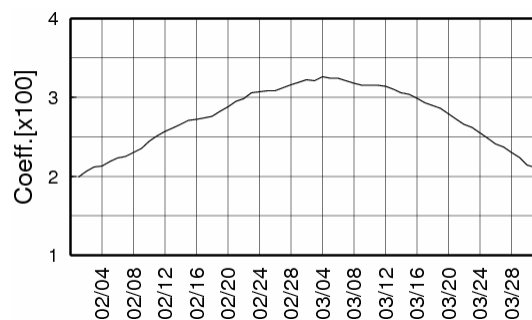


Figure 2. Time sequence of a bias correction coefficient in TEST for the same period as Figure 1.

References:

- Dee, D. P., 2004: Variational bias correction of radiance data in the ECMWF system. Proceedings of the ECMWF workshop on assimilation of high spectral resolution sounders in NWP, Reading, UK, 28 June - 1 July 2004.
- Derber, J. C., and W. -S. Wu 1998: The use of TOVS cloud-cleared radiances in the NCEP SSI analysis system. *Mon. Wea. Rev.*, **126**, 2287-2299.

Data Assimilation Experiments using CHAMP Refractivity Data

Hiromu SEKO¹, Yoshinori SHOJI¹, Masaru KUNII¹, Kazuo SAITO¹, Yuichi AOYAMA²

¹ Meteorological Research Institute, Japan Meteorological Agency, Tsukuba, Japan

² National Institute of Polar Research

1. Introduction Heavy rainfalls occur when a large amount of water vapor was supplied to rainfall systems. Middle-level dry air also enhances the convections due to the destabilizing of the convective stability. Because water vapor is one of important factors that control rainfall, the water vapor data is expected to improve the rainfall prediction when it is assimilated into the initial condition of numerical models. In this study, the vertical refractivity profile at the tangent point, which is the closest point on the path from GPS satellite and CHAMP, was used as assimilation data. However, there are two problems in the assimilation. (1) The resolution of refractivity data provided by GFZ is 200m. Generally, the data is thinned out to reduce the correlation of the observation error. However, the thinned data became the impact of data assimilation weaker. (2) Actual observed value is the integrated value along the path, because the CHAMP receives the signal that penetrated through the atmosphere. The tangent point value is estimated by using the assumption the refractivity is uniform in the horizontal direction. However, the refractivity does not always satisfy this assumption. Thus, the assimilation method of the high-resolution path-refractivity data should be developed.

2. Numerical model and refractivity data observed by CHAMP In this study, the refractivity data was assimilated into the Meso Spectrum Model (MSM) of Japan Meteorological Agency by using the Meso-4DVar Data Assimilation System (Koizumi et al., 2005). Firstly, the bias and RMSE of D-value, which is difference of observation and first guess value, was investigated by using the data of July 2004. Because the large bias existed below 2km, the data above the 2km was used in this study. The observation error of the tangent point data was also estimated from RMSE. Figure 1 shows the impact of the tangent point data. The small observation error was given to show the impact more clearly. When the CHAMP data was assimilated, the precipitation region became close to the observed one. This, the CHAMP data has the potential to improve the rainfall forecast. When the thinning was performed, the precipitation was not reproduced (not shown).

3. Vertical correlation of observation error The vertical correction of the observation error was estimated by following Chen et al. (2005). They assumed that D-value is sum of the deviations of forecast error and observation error. The deviation of the forecast error was estimated by NMC method (Parrish and Derber, 1992). The correlation coefficient was obtained from the deviation of observation error (fig. 2a), and then the correlation coefficient was simplified (fig. 2b). The observation error covariance was calculated by multiplying the observation error (fig. 2c). The observation error multiplied by 0.1 was used in the following experiments. When observation error covariance was used in the assimilation, the precipitation region was reproduced where they were observed (fig.3a). On the other hand, the precipitation was not reproduced when the vertical correlation was considered (fig. 3b).

4. Assimilation of path-refractivity data Figure 4 shows the schematic illustration of the path data. In the CASE 2, the path-averaged refractivity was assimilated. The path-averaged value was reproduced by the weighted average of the tangent point refractivity data. The weight is the path length within the layer of 200m. The observation error was also estimated by the same way from the observation error of tangent points. The modeled refractivity average was estimated by following procedures; (1) the path was divided into small elements. (2) refractivity at the center of elements was estimated from the grid point values. (3) the value of refractivity multiplied by the element length was added up and then divided by the path length. When the path-averaged value was assimilated, the impact of CHAMP data became smaller (fig. 5). It is deduced that the information of low level humid air was not used to moisten only the lower air in CASE2.

The vertical correlation of the path data is also considered in the same way as the tangent point. When the path-averaged refractivity was assimilated with consideration of the vertical correlation of observation error, the precipitation became stronger and became closer to the observed one (fig. 6).

Acknowledgments

CHAMP data were provided from GFZ. The initial and boundary conditions of MSM were provided from the Numerical Prediction Division (NPD) of JMA. We also used MSM and Meso-4DVar system developed by NPD/JMA. We would like to thank Dr. Wickert of GFZ and members of NPD/JMA.

References

- Chen, S.-Y., Y.-H. Kuo, S. Sokolovskiy and C.-Y. Huang, 2005: Estimation of observational errors of GPS radio occultation soundings. Second GPS RO Data Users Workshop, 22-24 August 2005, Lansdowne, USA.
- Parrish, D.F. and J.C. Derber, 1992: The national meteorological center's spectral statistical-interpolation analysis system. Mon. Wea. Rev., **120**, 1747-1763.

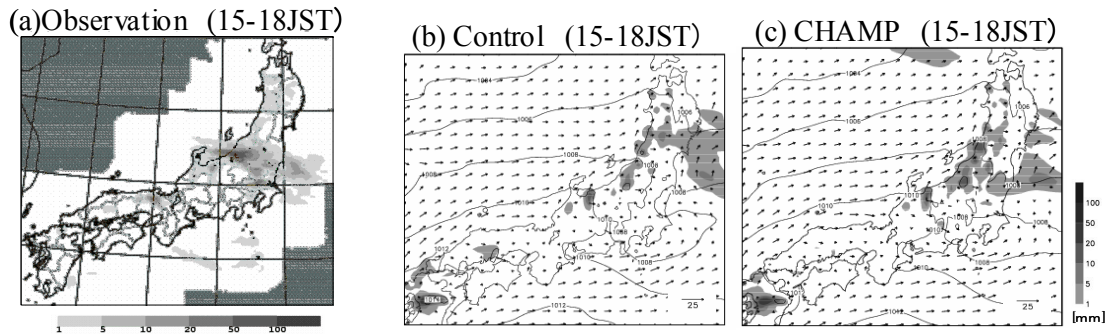


Fig.1 (a) Precipitation region observed by the convective radars from 15JST to 18JST on 16 July 2004. Shaded region in (b) and (c) indicate the precipitation region predicted by Meso-scale model from the analyzed fields. Analyzed fields were obtained by the assimilation of (b) conventional data and of (c) conventional data and CHAMP data

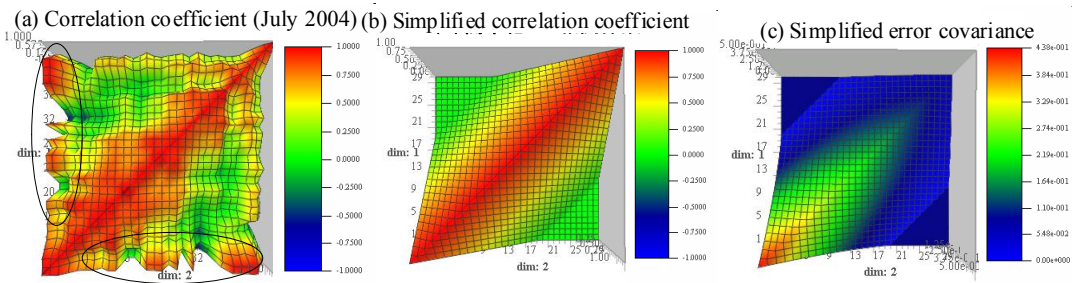


Fig. 2 (a) Vertical correlation of observation data, (b) simplified correlation and (c) observation error covariance. Observation error was estimated from the D-value of July 2004

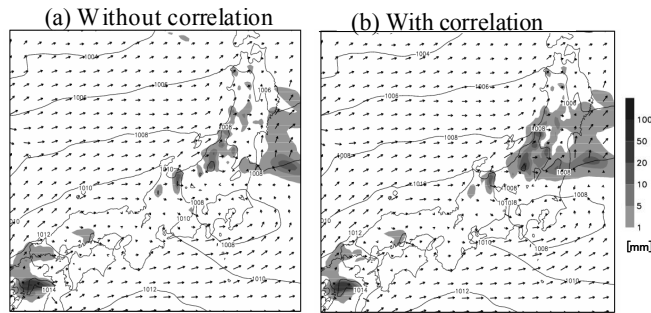


Fig. 3 Precipitation region predicted from the analyzed fields. Analyzed fields was obtained by the assimilation of refractivity data (a) without and (b) with consideration of the vertical correlation of the observation data.

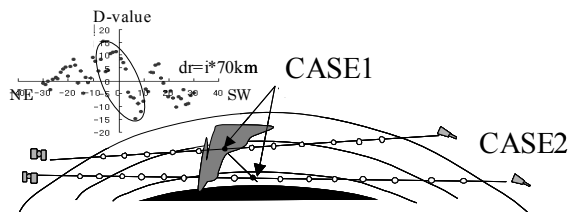


Fig. 4 Schematic illustration of positions of the assimilation data and (upper right) distribution of D-values along the observed path.

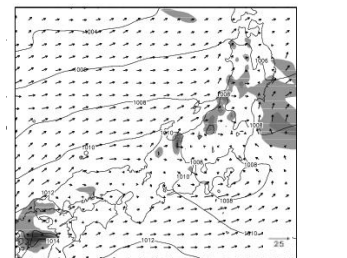


Fig. 5 Precipitation regions predicted from the analyzed fields. The analyzed fields were obtained by assimilation of CASE2.

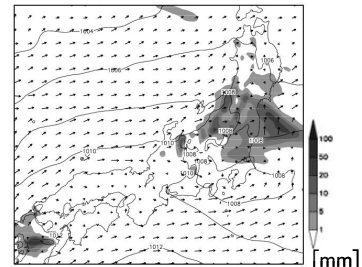


Fig. 6 Precipitation regions predicted from the analyzed fields. The analyzed fields were obtained by assimilation of CASE2 with the consideration of the vertical correlation of the observed data .

A covariance model based on 3-D spatial filters: potential for flow-dependent covariance modelling

M.D.Tsyrlunikov and P.I.Svirenko

Russian Hydrometeorological Center

E-mail: tsyrlunikov@mecom.ru

1 Introduction

In data assimilation, an advanced forecast (background) error covariance model is required to be capable of representing spatially variable and flow-dependent structures. These involve inhomogeneities in variances and decorrelation lengths: in the vertical, over latitude, between sea and land, dependent on the weather system etc. We also wish to model local horizontal anisotropies due to fronts, jet streams etc. Finally, vertically tilted structures typical for baroclinic zones are to be represented in the covariance model.

In this short contribution, we present a covariance model being developed in the Hydrometcentre of Russia and demonstrate its capability of modelling spatially variable structures. The univariate aspect is considered.

2 The covariance model

The covariance (stochastic) model is of the spatial auto-regression and moving-average (SARMA) type:

$$S\xi = V\alpha, \quad (1)$$

where ξ is the background-error field, α the driving white noise, S the spatial auto-regression linear filter, and V the spatial moving-average filter. Each of the two operators is defined by using discretized integral or differential operators (see below), giving rise to a *sparse* (and thus computationally efficient) matrix formulation.

In order to specify the S and V operators in Eq.(1) we propose the following construction. Because the vertical direction is the very special direction in the Earth's atmosphere (and ocean), we define S and V such that Eq.(1) is a *one-dimensional ARMA model in the vertical*, so that model Eq.(1) becomes

$$P_S(\partial/\partial z) \cdot \xi = P_V(\partial/\partial z) \cdot \alpha, \quad (2)$$

where z is the vertical coordinate, P_S and P_V are the polynomials whose coefficients are *horizontal operators*.

Examination of the 3-D ECMWF background-error covariances in (Tsyrlunikov 2001) suggested that (spectral) vertical correlations can be modelled with the Kagan's or degenerate 3-rd order auto-regression model. In view of this finding, we simplify the above model by defining P_S to be $(\partial/\partial z + T)^q$, where $q = 3$ and T is the horizontal operator. We define P_V to be a zero-order polynomial, $P_V = U$, where U is the horizontal operator. Thus, our stochastic model reads

$$\left(\frac{\partial}{\partial z} + T\right)^q \cdot \xi = U \cdot \alpha. \quad (3)$$

We have to synthesize the horizontal operators T and U that produce the desired 3-D covariance structure and also lead to a computationally efficient analysis algorithm. As for T , it appears to be possible to approximate it using a (very fast) finite-difference operator:

$$T = P_T(-\hat{\Delta}), \quad (4)$$

where P_T is the low-order polynomial and $\hat{\Delta}$ is a finite-difference approximation to the horizontal Laplacian. As for U , it appears to be more reasonable to approximate it with the discretized integral operator:

$$(U \cdot \alpha)(x) = \int u(\rho(x, y))\alpha(y)dy, \quad (5)$$

where x and y are points in the horizontal (spherical or plane) domain, ρ the distance between x and y , and $u(\rho)$ is the function that has *small* support to enforce sparse matrix algebra.

The above definition of the SARMA model is based on *operators* and thus is essentially coordinate-free, hence its applicability on any domain in any geometry. The model produces fully non-separable 3-D correlations.

3 Spatially variable covariances

Spatial variability can be introduced into model Eq.(3) by specifying spatially variable operators T and U . E.g., in Fig.1 we show a realization of the pseudo-random field (the horizontal cross-section) generated with model Eq.(3) in which the horizontal scale of $u(\rho)$ was intentionally decreased in a ‘cyclone’ located at 45N, 0E.

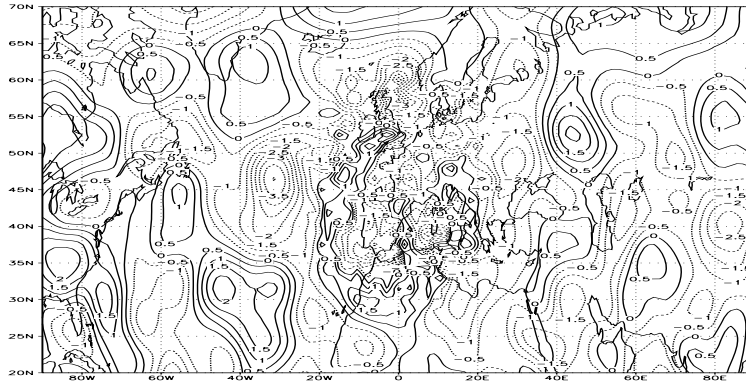


Figure 1: Horizontal inhomogeneity in the horizontal length scale. (the lat-lon cross-section)

Tilted structures are modelled by adding, in Eq.(3), to T , the term $\mathbf{c}\nabla$ (where \mathbf{c} is a horizontally variable horizontal vector and ∇ the horizontal gradient operator). The resulting pseudo-random field (for the case when \mathbf{c} is non-zero in the ‘cyclone’) looks as in Fig.2 (the vertical cross-section).

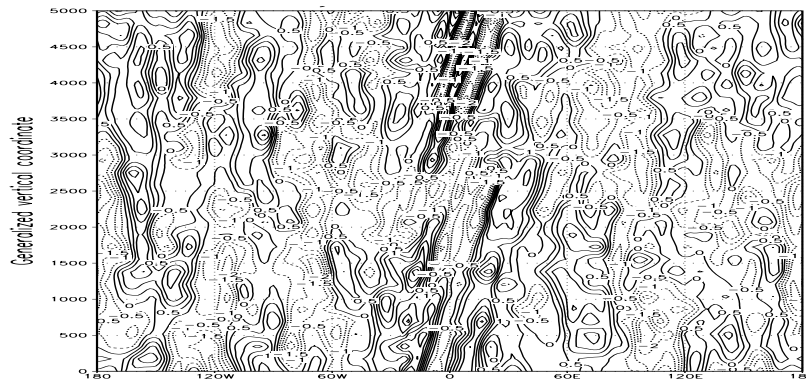


Figure 2: Modelling tilted structures (the longitude-height cross-section)

We would stress that any spatial (in particular, flow-dependent) variability introduced to model Eq.(3) cannot, by construction, violate positive definiteness of the resulting covariance matrices.

This study has been supported by the Russian Foundation for Basic Research under grant 06-05-08076.

REFERENCE

Tsyroulnikov M.D. Proportionality of scales: An isotropy-like property of geophysical fields. – *Q. J. R. Meteorol. Soc.*, 2001, **127**, 2741–2760.

Revised usage of Atmospheric Motion Vectors (AMV) from all geostationary satellites in the operational global 4D-Var assimilation system

Koji Yamashita

Japan Meteorological Agency / Numerical Prediction Division
1-3-4, Otemachi, Chiyoda-ku, Tokyo 100-8122, Japan
e-mail:kobo.yamashita@met.kishou.go.jp

A pre-processing system for Atmospheric Motion Vector (AMV) in the BUFR encoded dataset (BUFR AMV) generated from all geostationary satellites was revised in the JMA operational global 4D-Var assimilation system on 18 October 2006. Before the revision, BUFR AMVs from only METEOSAT satellites and SATOB AMVs from MTSAT-1R and GOES satellites had been assimilated in the global assimilation system. BUFR AMVs have a great advantage over SATOB AMVs in the high density distribution and the availability of quality information called QI (Quality Indicator). Thus we replaced all SATOB AMVs with corresponding BUFR AMVs in the global assimilation system. Furthermore, in order to use efficiently BUFR AMVs, we made several revisions of the pre-processing system for AMVs. First, the usage of the data is more strictly limited reflecting the error characteristics according to their heights. Secondly, fewer but more reliable data are assimilated by setting more rigorous QI threshold. Lastly, a new, intelligent thinning scheme is introduced to select the data, taking into account the QI and observation location and time, so that they are homogeneously distributed.

To assess the impacts of the new AMV scheme, one-month observation system experiments were performed for January 2006 and September 2005. The experiment for January 2006 demonstrates positive impacts on forecast skills in terms of the 500hPa geopotential height (Fig.1). Impacts of the other experiment are globally neutral for the 500hPa geopotential height, but positive for the surface pressure (not shown). In addition, the typhoon track predictions slightly improve as in Figure 2.

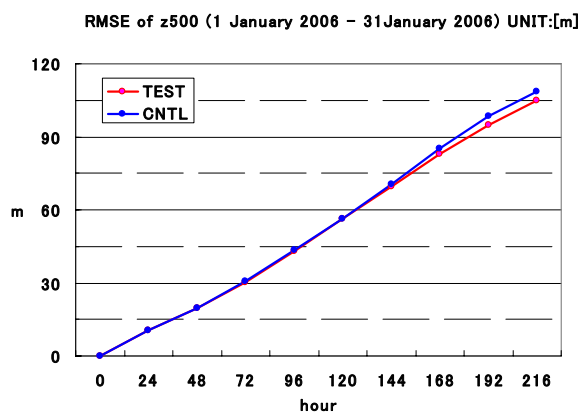


Figure 1 The global root mean square error (RMSE) for the 500hPa geopotential height verified against analysis. They are from 1st through 31st January 2006 for the new QC scheme (TEST) and the former scheme (CNTL).

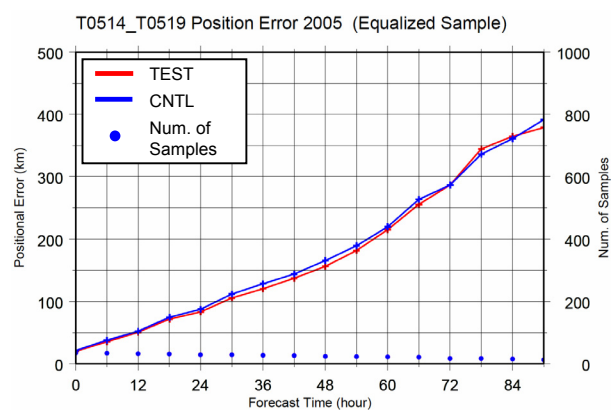


Figure 2 Averaged typhoon track error in September 2005. Blue dots indicate the number of cases used in this statistics.

